ADVANCED OPTICAL MATERIALS
www.advopticalmat.de

Optical Properties of Electrochemically Gated $La_{1-x}Sr_xCoO_{3-\delta}$ as a Topotactic Phase-Change Material

*Rohan D. Chakraborty, William M. Postiglione, Supriya Ghosh, K. Andre Mkhoyan, Chris Leighton, and Vivian E. Ferry**

Materials with tunable infrared refractive index changes have enabled active metasurfaces for novel control of optical circuits, thermal radiation, and more. Ion-gel-gated epitaxial films of the perovskite cobaltite $La_{1-x}Sr_xCoO_{3-\delta}$ (LSCO) with $0.00 \leq x \leq 0.70$ offer a new route to significant, voltage-tuned, nonvolatile refractive index modulation for infrared active metasurfaces, shown here through Kramers–Kronig-consistent dispersion models, structural and electronic transport characterization, and electromagnetic simulations before and after electrochemical reduction. As-grown perovskite films are high-index insulators for $x < 0.18$ but lossy metals for $x > 0.18$, due to a percolation insulator-metal transition. Positive-voltage gating of LSCO transistors with $x > 0.18$ reveals a metal-insulator transition from the metallic perovskite phase to a high-index ($n > 2.5$), low-loss insulating phase, accompanied by a perovskite to oxygen-vacancy-ordered brownmillerite transformation at high x. At $x < 0.18$, despite nominally insulating character, the LSCO films undergo remarkable refractive index changes to another lower-index, lower-loss insulating perovskite state with $\Delta n > 0.6$. In simulations of plasmonic metasurfaces, these metal-insulator and insulator-insulator transitions support significant, varied mid-infrared reflectance modulation, thus framing electrochemically gated LSCO as a diverse library of room-temperature phase-change materials for applications including dynamic thermal imaging, camouflage, and optical memories.

1. Introduction

Optical metasurfaces have enabled unprecedented nanoscale control over light-matter interactions, supporting exotic phenomena such as negative refractive index[1,2] and subwavelength "flat" optics.[3] While traditional metasurfaces have a fixed geometry and therefore a static optical response, it is possible to add active tunability to these systems by pairing them with materials that undergo controllable refractive index changes to create active metasurfaces.[4,5] Various modulation mechanisms and materials have been used to achieve this tunability, including electrostatic modulation in materials like transparent conducting oxides[6–9] and graphene,[10,11] thermally-mediated phase changes in $Ge_xSb_yTe_z$ (GST)[12–18] and VO_2,[19–23] electro- and photochromic materials,[24–28] nonlinear materials,[29] and liquid crystals.[30,31] Collectively, these tunable materials systems have enabled dynamic behavior such as reflection[15,19,25] and transmission[8,23] modulations, color switching,[24,31] and high-efficiency beam steering,[9,12–14] with numerous applications in the visible and infrared. The phase-change materials VO_2 and GST have been especially popular for infrared applications, including telecommunications[12–14,19–21,23] and thermal imaging,[15,16] due to their significant refractive index changes in the near- and mid-infrared. VO_2 undergoes a monoclinic-to-rutile transformation at 68 °C, where the room-temperature insulating phase shows high index and low loss, while the high-temperature metallic phase is highly lossy.[32,33] In contrast to VO_2's insulator-metal transition, GST alloys undergo a nonvolatile, thermally induced amorphous-to-crystalline phase transition between two distinct high-index insulating phases.[12,16,17] However, phase-change materials like VO_2 and GST can be difficult to work with due to the volatile nature of VO_2's phase transition (when thermally induced) and the elevated temperatures required to induce phase transitions in these materials (68 °C for the VO_2 insulator-metal transition,[19,20,22] over 150 °C for GST crystallization,[12,15] and over 600 °C for GST amorphization[13,18]). In active metamaterial devices, this necessitates the use of thermal annealing,[12,15,20] resistive heating,[13,14,19] or pulsed lasers[16,18] to induce the phase change. These challenges with VO_2 and GST motivate the search for alternative materials that undergo both nonvolatile and low-power refractive index changes.

Another technique that can significantly modulate material properties is electrolyte gating.[34–36] Here, the traditional gate

R. D. Chakraborty, W. M. Postiglione, S. Ghosh, K. A. Mkhoyan, C. Leighton, V. E. Ferry
Department of Chemical Engineering and Materials Science
University of Minnesota
421 Washington Avenue SE, Minneapolis, MN 55455, USA
E-mail: veferry@umn.edu

The ORCID identification number(s) for the author(s) of this article can be found under https://doi.org/10.1002/adom.202300098

DOI: 10.1002/adom.202300098

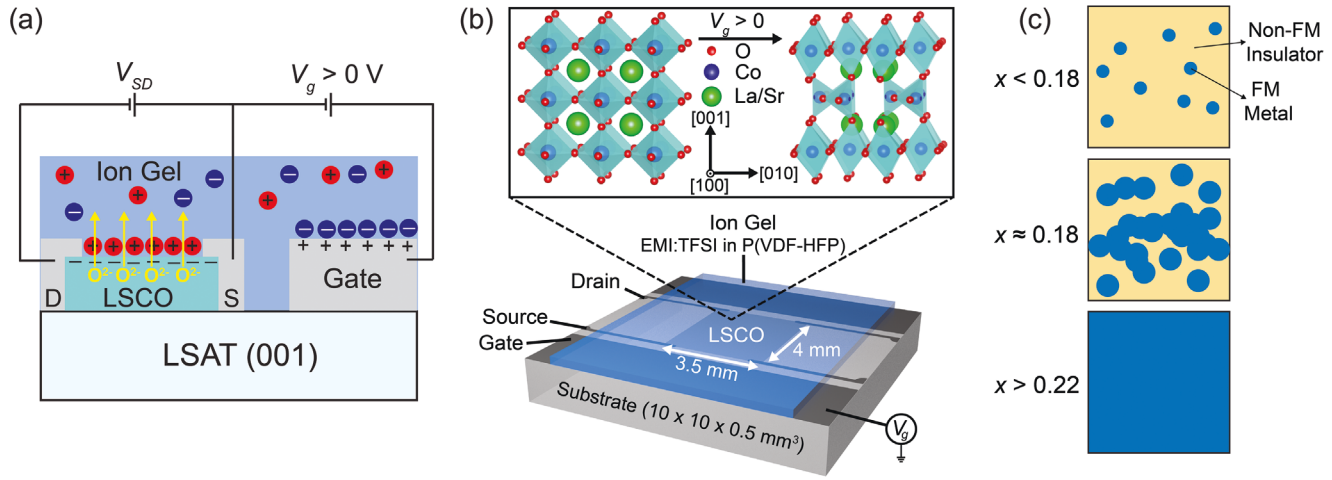

Figure 1. a) Schematic of a side-gated ion-gel transistor based on an epitaxial $La_{1-x}Sr_xCoO_{3-\delta}$ (LSCO) film on an LSAT(001) substrate operating under positive gate voltage ($V_g > 0$ V), at a fixed source-drain voltage (V_{SD}). Oxygen migrates out of the film, forming oxygen vacancies, as shown. Source and drain electrodes are denoted (S) and (D), respectively. b) 3D schematic of the specific side-gated ion-gel transistors used in this study. Inset: Topotactic perovskite (P) to oxygen-vacancy-ordered brownmillerite (BM) transformation in LSCO ion-gel-gated transistors under positive gate voltage ($V_g > 0$ V); pseudocubic axes are shown. c) Schematic of the percolation insulator-metal transition in bulk perovskite LSCO. LSCO is insulating with small metallic ferromagnetic clusters (blue) for $x < 0.18$ (top panel), followed by cluster percolation at $x = 0.18$ (middle panel), followed by a uniform metallic, ferromagnetic ground state at $x > 0.22$ (bottom panel).

oxides in transistors are replaced with high-specific-capacitance (≈10 μF cm^{-2}) ionic liquids or ion gels (i.e., ionic liquids embedded in solid-state polymer networks) and the application of a moderate gate voltage (V_g) induces large electric fields at the interface between the target material and the electrolyte due to the formation of nanoscale electric double layers.[34–36] As a result, electrolyte gating has enabled dramatic voltage-driven modulation of electronic, magnetic, and optical properties, in systems such as 2D materials,[37,38] organic semiconductors,[39,40] and oxides.[25,34–36,41–45] Critically, it is now understood that the operation of such devices can be electrostatic (via induction of electrons/holes), or electrochemical, but both can be reversible.[34,35] In oxides, for example, the interfacial electric field can remove or insert oxygen ions (depending on the V_g polarity), generating a nonvolatile but reversible redox-based voltage response.[34,35]

The perovskite cobaltite $La_{1-x}Sr_xCoO_{3-\delta}$ (LSCO) has been the subject of particularly intensive electrolyte gating studies.[46–48] LSCO exhibits an attractive combination of high room-temperature diffusivity of oxygen vacancies (≥ 100 nm diffusion lengths at room temperature on minute time scales),[48] coupled with low formation enthalpies of these vacancies.[48] The formation enthalpy decreases with x, due to the instability of Co as it approaches 4+ formal valence in octahedral coordination.[48–50] These properties lead to enhanced electrochemical response during electrolyte gating. As shown in **Figure 1**a, the application of positive V_g induces electrochemistry, the electric field at the LSCO/ion gel interface facilitating the formation and migration of oxygen vacancies, leading to reduction and substantial property modulation. This mechanism and its associated non-volatility have been confirmed with numerous techniques, including *operando* synchrotron X-ray diffraction and electronic transport.[46–48] More recent electrolyte gating studies of LSCO explored higher positive V_g, inspired by the electrolyte-gate-driven topotactic phase transformation of $SrCoO_{3-\delta}$ (SCO, i.e., $x = 1$ LSCO) between its metallic, ferromagnetic perovskite (P) phase, $SrCoO_3$, and its insulating, antiferromagnetic, oxygen-vacancy-ordered, brownmillerite (BM) phase, $SrCoO_{2.5}$[43,51,52] as depicted in Figure 1b. The BM phase of $SrCoO_{3-\delta}$ is structurally very different from the P phase, exhibiting alternating (001) planes of tetrahedrally- and octahedrally-coordinated Co ions[43,51,52] due to the oxygen vacancy order, and thus strikingly different electronic and magnetic properties. Notably, this voltage-driven phase transformation can be cycled reversibly, where positive V_g drives to the BM phase and negative V_g drives to the P phase.[43,51,52] The filling of oxygen vacancies required for reversible reoxidation is thought to be enabled by the electrolysis of residual water in the ionic liquids and gels used.[51] Important in the current context, recent work of our own established that this V_g-driven P → BM transition is general to the LSCO system, not only in SCO ($x = 1$), but at various x (e.g., $x = 0.50$), as confirmed by *operando* synchrotron diffraction, electronic transport, magnetometry, and optical transmittance measurements.[48] This is important for potential applications, as LSCO has significantly enhanced air stability of both the P and BM phases relative to SCO, while x provides a useful knob to tune the phase transformation threshold voltage.[48] Also of importance is that LSCO's P ↔ BM transformation is likely cyclable on ~Hz time scales, as returned to below, analogous to the reversible tuning already established in SCO.[43,51,52]

What is clearly lacking from the above studies of electrochemically gated LSCO is a thorough understanding of the optical properties in films with different x, both before and after positive-V_g gating. First, the refractive index of P LSCO is expected to vary substantially with x due to a percolative insulator-metal transition,[50,53] illustrated in Figure 1c. At $x = 0$, bulk $LaCoO_3$ (LCO) is a diamagnetic insulator at low temperature, but as the Sr doping is increased the substitution of Sr^{2+} for La^{3+} leads to the formation of short-range clusters of a metallic

ferromagnetic phase (Figure 1c, top panel). At $x \approx 0.18$, these metallic clusters reach percolation, driving an insulator-metal transition (Figure 1c, middle panel), resulting in a uniform ferromagnetic, metallic ground state at sufficiently high x (Figure 1c, bottom panel).[50,53] While this picture is consistent with the well-studied x-dependent electronic transport properties of bulk LSCO,[50,53] optical studies of this percolative transition are limited. Optical conductivity measurements on bulk LSCO show a transition from low-to-high infrared absorption with increasing x, corresponding to the closing of an electronic bandgap, but only exists up to $x = 0.30$.[54,55] Meanwhile, thin-film optical studies only exist for LSCO at $x = 0$[56,57] and 0.50.[58] Perhaps most remarkable, however, is that V_g-driven changes in LSCO films at various x have not been considered for tunable nanophotonic applications such as active metasurfaces. In fact, electrolyte gating itself has rarely been applied to metasurfaces, with only two reported cases of electrochemical induction of insulator-metal transitions in VO_2[59] and $SmNiO_3$[25] for metasurface applications.

In light of the above, here we report systematic visible-to-mid-infrared complex refractive index studies of LSCO films across nearly the entire phase diagram (x = 0.00, 0.10, 0.28, 0.50, and 0.70), both before and after electrochemical gating at V_g = +3.5 V. The gating is performed with an ion gel electrolyte made of 1-ethyl-3-methylimidazolium bis(trifluoromethylsulfonyl)amide (EMI:TFSI) (an ionic liquid) dispersed in poly(vinylidene fluoride-co-hexafluoropropylene) (P(VDF-HFP)). In as-grown perovskite films, Kramers-Kronig-consistent refractive index models reveal gapped, insulating behavior at $x = 0$ and 0.10, and highly absorbing metallic behavior at $x = 0.28$, 0.50, and 0.70, consistent with the expected percolation insulator-metal transition. We then show that LSCO films with $x \geq 0.28$ transform from highly lossy metallic phases to high-index, low-loss insulators (especially in the infrared) upon electrochemical gating, accompanied by a P → BM topotactic transformation for $x = 0.50$ and 0.70. LSCO films with $x \leq 0.10$ also undergo significant refractive index changes between two high-index insulating states when gated. LSCO is thus capable of both metal-insulator and insulator-insulator phase-change via electrochemically induced formation and migration of oxygen vacancies, depending on the Sr doping, but with refractive index changes that are nonvolatile, relatively low power consumption (i.e., both the gate voltage and gate current are low), and accessible at room temperature.

2. Results and Discussion

2.1. Structural and Electronic Characterization of Perovskite LSCO

We begin our analysis with the characterization of our as-deposited epitaxial P LSCO films, first through X-ray diffraction (XRD) and electronic transport measurements. **Figure 2**a shows specular XRD scans of heteroepitaxial, tensile-strained LSCO films with in-plane strain (ϵ_{xx}) of $0.8\% \leq \epsilon_{xx} \leq 1.5\%$ grown on $(LaAlO_3)_{0.3}(Sr_2TaAlO_6)_{0.7}$ (LSAT) 001-oriented substrates, at all five compositions ($x = 0$, 0.10, 0.28, 0.50, 0.70) studied here. The LSAT 002 reflections and well-defined P LSCO 002 reflections (with prominent Laue oscillations) are seen at all x. Small differences in LSCO peak widths and Laue oscillation periods occur,

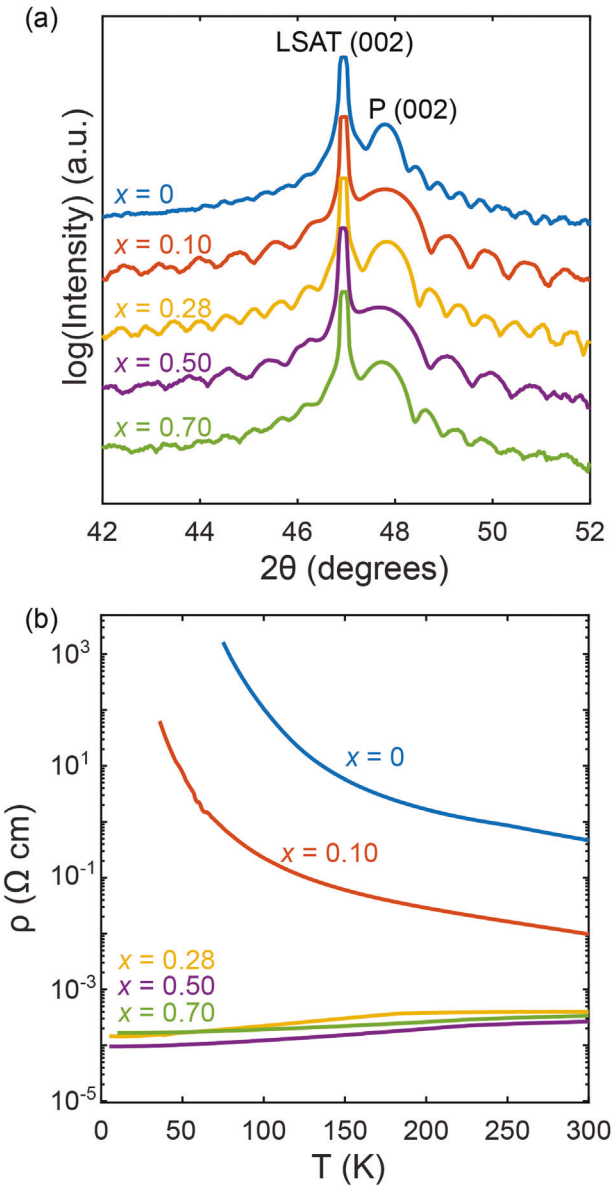

Figure 2. a) High-resolution specular X-ray diffraction scans of 12–22 nm-thick perovskite LSCO films at x = 0, 0.10, 0.28, 0.50, and 0.70 on LSAT(001) substrates, showing the P LSCO 002 reflections present at all x. Scans are offset for clarity. Differences in Laue fringe intensity between scans are due to sample-to-sample variations in roughness. b) Temperature-dependent resistivity of the same LSCO films at x = 0, 0.10, 0.28, 0.50, and 0.70, again on LSAT(001) substrates. The resistivity curve for $x = 0$ is the same as that in Chaturvedi et al.[62]

but these are simply due to differences in film thickness across the compositions (12–22 nm); our prior studies with reciprocal space mapping clearly confirm full-strain to the LSAT substrates at these thicknesses.[60] Consistent with the Laue oscillations seen here, and extensive prior characterization, these films have low surface/interface roughness and are phase-pure.[48,60–63] In Figure 2b, we highlight the corresponding temperature (T)-dependent resistivity (ρ) of these LSCO films, which shows the percolation insulator-metal transition expected for P LSCO. At

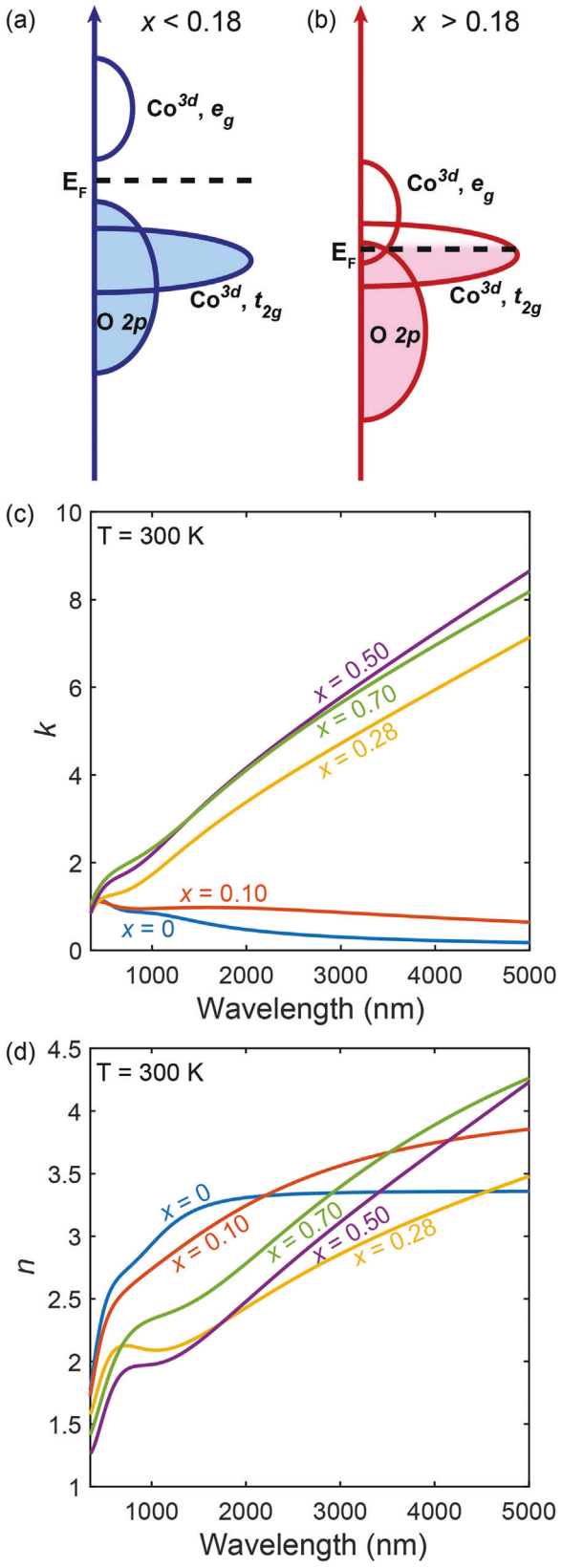

Figure 3. a) Representative sketch of the room-temperature density-of-states of the various bands near the Fermi level (E_F) in insulating perovskite LSCO ($x < 0.18$). b) Representative sketch of the room-temperature density-of-states of the various bands near the Fermi level for metallic perovskite LSCO ($x > 0.18$). c) Imaginary and d) real parts of the 300-K wavelength-dependent complex refractive index of as-grown perovskite LSCO films at all x studied, obtained from fitting room-temperature spectroscopic ellipsometry and optical transmittance data to Kramers–Kronig dispersion models (see Table S1, Figures S1 and S2, Supporting Information).

$x = 0$ and 0.10, P LSCO films display clearly insulating behavior, but the $x = 0.10$ films have room-temperature resistivity nearly two orders of magnitude lower than at $x = 0$, due to hole doping. Consistent with the $x = 0.18$ percolation threshold,[50,53] $x = 0.28$ LSCO has much lower resistivity, now with a positive temperature coefficient of resistivity, indicating clearly metallic behavior (the slope changes near 175–250 K reflect the ferromagnetic Curie temperature). As x is further increased, $\rho(T)$ maintains a similar shape and decreases to $x = 0.50$, before increasing slightly at $x = 0.70$. This nonmonotonicity at high x has also been seen in bulk LSCO,[50] and occurs due to redox instability as x exceeds ≈0.50, resulting in oxygen vacancies that compensate the Sr doped holes.[48–50,60,64]

2.2. Optical Characterization of Perovskite LSCO

We begin our optical characterization of P LSCO by discussing, separately for insulating ($x < 0.18$) and metallic ($x > 0.18$) compositions, the relevant electronic transitions expected. **Figure 3**a shows a qualitative, representative illustration of the density-of-states of the bands near the Fermi energy (E_F) in $x = 0$ LSCO (LCO), constructed in reference to prior experimental and computational studies of bulk and thin-film LCO.[56,57,62,65,66] This picture is designed to be consistent with the expected insulating nature of LCO at room temperature, with the known O^{2p}-Co^{3d} e_g interband transition spanning ≈2.0–3.2 eV, and with the known Co^{3d} t_{2g}-e_g intraband transition spanning ≈1.0–2.0 eV; these are the two main electronic transitions observed in the visible to mid-infrared range.[56,57,67,68] Similarly, Figure 3b shows a representative equivalent schematic for $x > 0.18$ (i.e., metallic) LSCO at room temperature (in the paramagnetic state), constructed in reference to experimental and computational studies of LSCO and perovskite $SrCoO_{3-\delta}$ (P SCO).[51,54,55,69–71] Here, our depiction is designed to capture the experimental observations of an O^{2p}-Co^{3d} interband transition in the visible and a Co^{3d} t_{2g}-e_g Drude transition in the infrared ($\lesssim$ 1.0 eV).[51,54,55,58,69,71] We also acknowledge that O^{2p} holes have been discussed to exist at the E_F in $x > 0.18$ LSCO, and we have incorporated this detail into our schematic.[72,73]

The rest of Figure 3 shows our room-temperature Kramers–Kronig-consistent complex refractive index models for as-deposited P LSCO films with $0 \leq x \leq 0.70$, where the wavelength-dependent imaginary refractive index (k) is shown in Figure 3c and the real index (n) is shown in Figure 3d. Further details of the techniques and measurements used to generate these refractive index models are provided in the Experimental Section and the Supporting Information. Because changes in LSCO's electronic structure are directly reflected in light absorption trends (i.e., trends in k), we first focus our analysis on Figure 3c. Here, LCO ($x = 0$ LSCO) has an imaginary index that decreases with

wavelength, showing two absorption features centered at ≈400 and ≈1000 nm. This imaginary index for LCO shows excellent qualitative and quantitative agreement with previous experimental studies of LCO and with the diagram in Figure 3a, specifically a stronger and narrower absorption peak at higher photon energy (≈400 nm) due to the O^{2p}-Co^{3d} e_g transition, and a weaker but broader absorption peak at lower photon energy (≈1000 nm) due to the Co^{3d} t_{2g}-e_g intraband transition.[54–57,67,68] Moving to x = 0.10 LSCO, we observe a similar spectrum overall, with a slight reduction in the magnitude of the peak near 400 nm, and significant increases in both the magnitude and width of the longer-wavelength absorption peak, attributed to metallic cluster formation due to Sr doping (Figure 1c, top panel). The light absorption in x = 0.28 LSCO is then consistent with metallic cluster percolation (Figure 1c, middle panel). The shorter-wavelength interband absorption feature is retained (as expected from the picture in Figure 3b), but the longer-wavelength absorption increases with wavelength and is much stronger in magnitude, indicating free-carrier Drude light absorption from the Co^{3d} t_{2g}-e_g intraband transition.[54,55] Considering the x = 0, 0.10, and 0.28 compositions together, we also note the slight decrease in the shorter-wavelength absorption feature, and the increase and broadening of the longer-wavelength feature, with x. We attribute this spectral weight transfer to a filling-controlled insulator-metal transition, previously described in terms of a Mott insulator-to-metal transition.[54,55] Through imaginary index trends observed in P LSCO at x = 0, 0.10, and 0.28, we thus observe optical signatures of the percolation insulator-metal transition, where the insulating ground state in LCO gives way to more optically lossy (but still insulating) behavior at x = 0.10, and finally to the onset of metallic, Drude absorption at x = 0.28. These findings are consistent with both our established theoretical picture (Figure 1c) and the measured $\rho(T)$ at different x (Figure 2b).

Moving to light absorption at higher x, Figure 3c shows a notable increase in k from x = 0.28 to 0.50, in agreement with the decrease in resistivity in Figure 2b. The magnitude and overall shape of the refractive index are also similar to prior refractive index measurements of x = 0.50 LSCO films, some of which used similar Drude–Lorentz refractive index models.[58] Finally, x = 0.70 LSCO shows a slight decrease in k relative to x = 0.50 at longer infrared wavelengths, but higher k at shorter wavelengths. As discussed in Figure 2b, this decrease in longer-wavelength light absorption is due to the valence instability of Co at x = 0.70 and the subsequent formation of oxygen vacancies that compensate doped holes.[48–50,60,64] Overall, the trends in the imaginary refractive index in Figure 3c capture the relevant electronic transitions expected in LSCO across the studied Sr doping window.

In Figure 3d, we present the corresponding real refractive index (n) of P LSCO films, where the magnitude and shape of n are directly linked to that of k (Figure 3c) via the Kramers–Kronig relations. For x = 0, we see that n increases significantly between ≈350 and 1500 nm, with shoulders around 600 and 1100 nm, then increases more slowly between 1500–5000 nm, finally leveling off at $n \approx 3.35$. Based on the Kramers–Kronig relations, the two shoulders observed in the n of LCO are attributed to the two absorption features in k at similar wavelengths, while the decreasing dispersion at longer wavelengths is attributed to the general decrease in absorption at those wavelengths. LSCO at x = 0.10 also shows stronger dispersion in the visible than in the infrared, but greater overall dispersion than LCO, due to stronger absorption throughout the infrared. The x = 0.28, 0.50, and 0.70 LSCO then show higher dispersion in n compared to the insulating compositions (x = 0 and 0.10) due to strong free-carrier light absorption (k) in the infrared. When we compare LSCO at x = 0.28 and 0.50 specifically, we see that x = 0.50 LSCO has comparatively smaller n at wavelengths below 1800 nm, but larger n at longer wavelengths, most likely due to the interband-to-intraband spectral weight transfer observed in k. This trend should also extend to x = 0.70 but is partly obscured by the redox instability of Co at high x. As a final note on this Kramers–Kronig-based analysis, we emphasize that there are certainly higher-energy interband absorptions in LSCO at wavelengths below 350 nm, as well as phonon-polaritonic modes at wavelengths above 5000 nm,[54,55] and that incorporating those absorption features in our analysis might slightly change the magnitudes of the refractive indices.

2.3. Electrolyte-Gating-Induced Electronic and Structural Changes in LSCO

Having characterized the complex refractive index of as-deposited P LSCO films, we now discuss the electrochemical gating of these films. **Figure 4**a first shows the 300-K source-drain current (I_{SD}) and gate current (I_g) in electrolyte-gated films of LSCO at various x as V_g is swept (at 0.50 mV s^{-1}) from 0 to 3.5 V. In general, LSCO films at all x exhibit lower I_{SD} (top panel) as gating proceeds to 3.5 V, indicating the expected increases in resistivity due to oxygen vacancy formation and proliferation. However, I_{SD} decreases by less than an order of magnitude with gating in LCO films, while decreasing by 3 orders of magnitude in x = 0.10 LSCO films, and finally almost 5 orders of magnitude for x = 0.28, 0.50, and 0.70 films. Some of the $I_{SD}(V_g)$ curves in Figure 4a also display clear features, such as abrupt slope changes at specific V_g values. In general, these slope changes coincide with local maxima in I_g at the same voltages, emphasizing that electrochemical activity is occurring at these points in the V_g sweep. More specifically, the features in I_{SD} and I_g mark the onset of oxygen vacancy formation and the transformation to BM, as we will detail in a future paper.[74] We also draw attention to the overall low I_g magnitude (< 500 nA cm^{-2}) for all x during the sweep, confirming the insulating nature of our ion gel. Complementary to Figure 4a, Figure 4b shows 300-K four-wire resistivity measurements of LSCO films before (V_g = 0 V) and after (V_g = 3.5 V) gating. Consistent with Figure 2b, the resistivity in the as-grown P phase decreases quickly from x = 0 to x = 0.50, before increasing slightly at x = 0.70. After gating, however, LSCO films with x = 0, 0.10, and 0.28 show nearly identical resistivity of ≈10 Ω cm, while gated films with x = 0.50 and 0.70 show noticeably higher resistivities of 29–31 Ω cm. These findings broadly agree with the results in Figure 4a, where the overall decrease in I_{SD} with V_g increases significantly from x = 0 to 0.10, then becomes largest at x = 0.50.

In order to map the above transport results to the relevant phase evolution, Figure 4c–f shows XRD and cross-sectional scanning transmission electron microscopy (STEM) results before and after gating. Focusing first on x = 0.50 and 0.70 films, Figure 4c shows specular XRD scans before (V_g = 0, black) and after (V_g = 3.5 V, purple and green, respectively) gating.

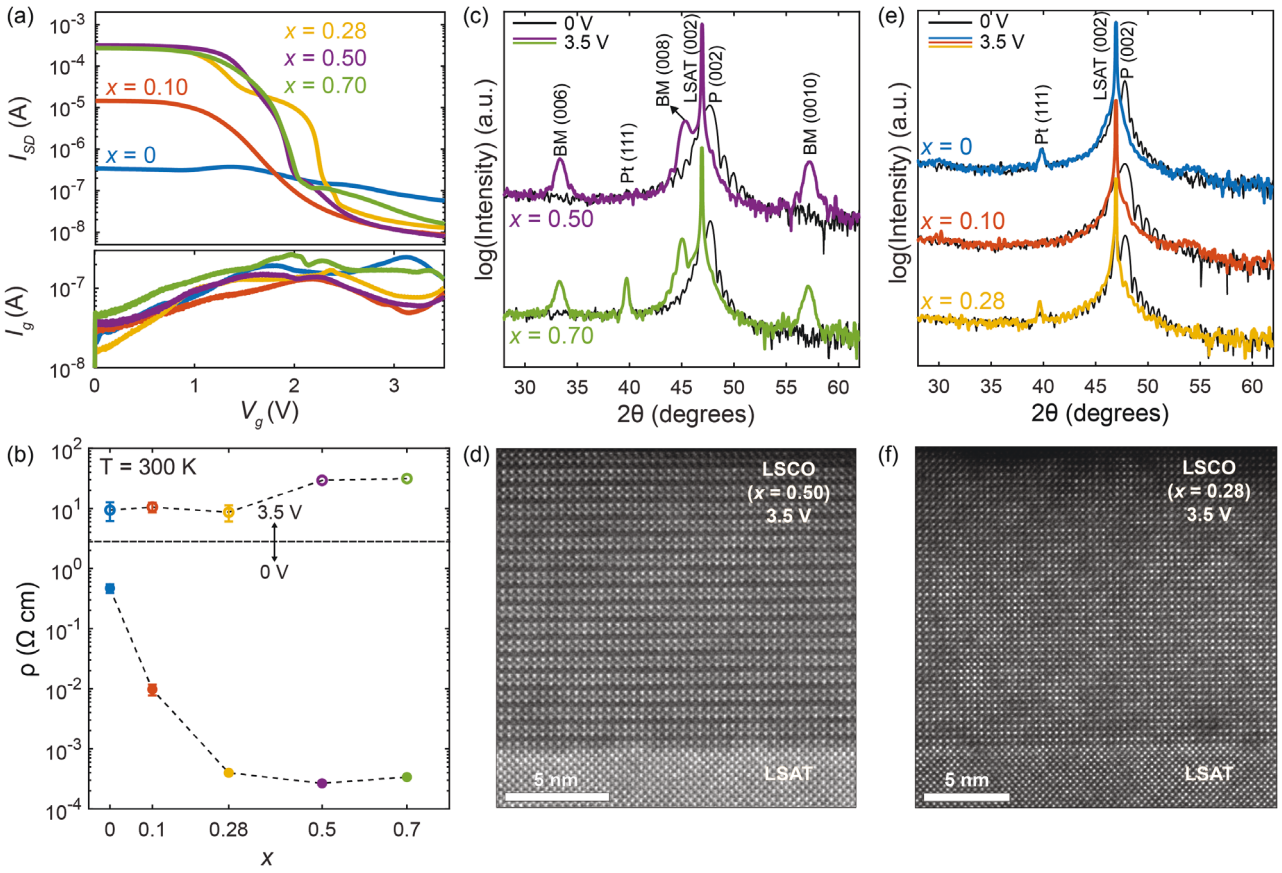

Figure 4. a) Gate voltage (V_g) dependence of the 300-K source-drain current (I_{SD}) (top panel) and 300-K gate current (I_g) (bottom panel) in ion-gel-gated LSCO films at various x, as V_g is swept from 0 to 3.5 V at a rate of 0.5 mV s^{-1}. b) Sr doping (x) dependence of the 300-K four-terminal resistivity of LSCO films at x = 0, 0.10, 0.28, 0.50, and 0.70 before (V_g = 0 V, closed symbols) and after (V_g = 3.5 V, open symbols) gating. The dashed lines connect data points, and error bars are shown for cases where the error is larger than the data points themselves. For as-grown LSCO films (0 V), the error bars represent the standard deviation between multiple samples. For gated LSCO films (3.5 V), the error bars represent the sum of systematic and random measurement uncertainty. c) High-resolution specular XRD scans of as-grown (V_g = 0) and gated (V_g = 3.5 V) LSCO at x = 0.50 and 0.70. d) Atomic-resolution HAADF-STEM image of gated (V_g = 3.5 V) LSCO at x = 0.50 at the film/substrate interface. e) High-resolution specular XRD scans of as-grown (V_g = 0) and gated (V_g = 3.5 V) LSCO at x = 0, 0.10, and 0.28. f) Atomic-resolution HAADF-STEM image of gated (V_g = 3.5 V) LSCO at x = 0.28 at the film/substrate interface.

The peaks at ≈33° and 57° after gating (the BM 006 and 0010 peaks, respectively) clearly evidence a transformation to the BM structure. Simultaneously, the primary P 002 film peak reduces slightly in intensity and shifts to a lower angle, transforming into the 008 peak of the BM structure (the unit cell is quadrupled out-of-plane). Similar gate-induced P → BM transformations were reported in our previous work[48] in x = 0.50 LSCO and in BM SCO.[51,52] (Note that the Pt 111 peaks in Figure 4c arise from the device electrodes [see Figure 1b]). These gated x = 0.50 and 0.70 LSCO films are in fact phase-pure BM, as emphasized in Figure S3, Supporting Information via comparisons to as-grown BM SCO films and quantitative analyses of peak intensity ratios. The long-range oxygen vacancy order characteristic of the BM structure is also evident in atomic-resolution high-angle annular dark field (HAADF) STEM images of gated x = 0.50 LSCO films, as shown in Figure 4d, where the alternating lines of horizontal light and dark contrast correspond to the oxygen-sufficient Co-O octahedral planes and oxygen-deficient Co-O tetrahedral planes of the BM structure (Figure 1b).

In clear contrast, the XRD scans in Figure 4e reveal no obvious BM peaks in gated films with $x \leq 0.28$. The P 002 film peaks do downshift into the LSAT 002 peak, however (see Figure S4, Supporting Information for more detailed confirmation of this point), indicating substantial increases in the P out-of-plane lattice parameter, meaning that significant oxygen vacancy creation has taken place. The electrochemically generated oxygen vacancies in gated films with $x \leq 0.28$ are thus disordered, in the P phase, while those in gated films with $x \geq 0.50$ are ordered, in the BM phase. Interestingly, the overlap of the P 002 film and P 002 LSAT substrate peaks in Figure 4e indicates that the films have assumed near-ideal cubic symmetry, as in-plane lattice parameter matching is known to be maintained in LSCO after electrolyte gating,[51] and the out-of-plane lattice parameter now matches that of the substrate. It is thus possible that symmetry matching plays a role in stabilizing this structure and the associated oxygen stoichiometry. In agreement with Figure 4e, the HAADF-STEM images of gated x = 0.28 LSCO in Figure 4f reveal no long-range oxygen vacancy ordering (compare to Figure 4d), instead showing

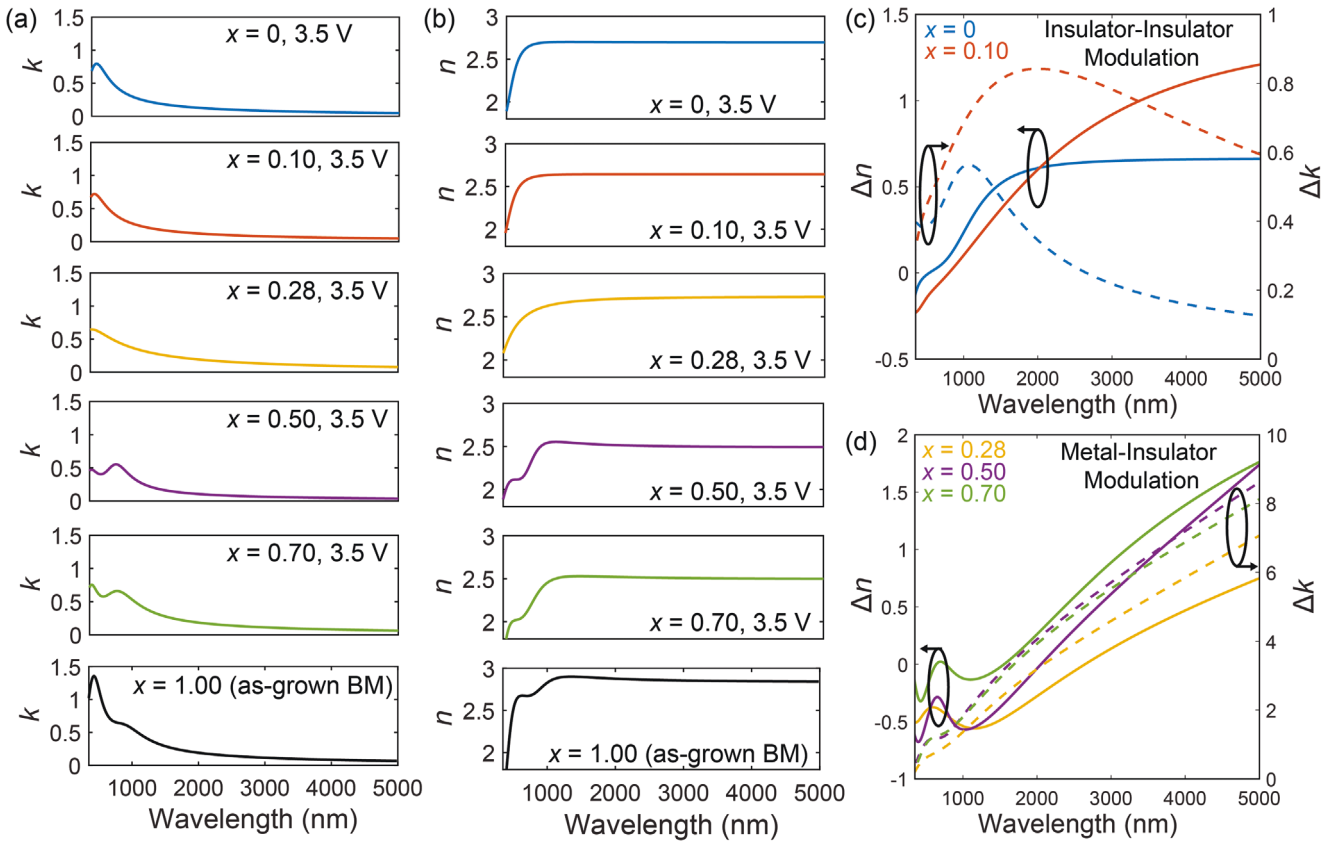

Figure 5. a) Imaginary and b) real parts of the wavelength-dependent complex refractive index of gated (V_g = 3.5 V) LSCO films ($0 \le x \le 0.70$), along with an as-grown brownmillerite SCO film (x = 1.00) for comparison (black, bottom panels). c) and d) show the difference in real (Δn, solid lines) and imaginary (Δk, dashed lines) parts of the refractive index between as-grown (V_g = 0 V) and gated (V_g = 3.5 V) LSCO for compositions that show insulator-insulator (x = 0 and 0.10) and metal-insulator (x = 0.28, 0.50, and 0.70) refractive index modulation, respectively. The black circles with arrows serve as guides to the eye.

isolated local regions with variable contrast, potentially indicating short-range oxygen vacancy ordering. In prior work at $x = 0$, we speculated on such short-range oxygen vacancy ordering or Grenier phase formation,[48] and, interestingly, broad, low-intensity features do arise around 29° and 55° in Figure 4e. While definitive proof of short-range oxygen vacancy order in lower x films remains to be established, the clear conclusion from Figure 4c,d is a V_g-driven P → BM transformation in LSCO films with x = 0.50 and 0.70, explaining the large modulation in I_{SD} and ρ in these cases (Figure 4a,b). The distinctly lower ρ after gating for x = 0, 0.10 and 0.28 films (Figure 4b) is then simply due to a gate-induced increase in oxygen vacancy concentration, but incomplete vacancy ordering into the BM structure. In essence, there thus exists a critical x^* (i.e., a critical level of redox instability) in order to gate LSCO to the fully-ordered BM phase, at least under the gating conditions and substrate choice employed here.

2.4. Optical Characterization of Electrochemically Gated LSCO

For the remainder of this study, we return to optical properties, beginning with the characterization of the refractive index of electrochemically gated LSCO at all x, as shown in **Figure 5**a,b. To aid in this analysis, we also include measurements of an as-grown BM SCO (x = 1.00) film in the bottom panels of Figure 5a,b. We note immediately that, at all x, gated LSCO films show significant changes in both k and n relative to P LSCO (Figure 3c,d), with all gated LSCO films showing insulating behavior. Electrochemical gating of LSCO films thus produces insulator-insulator refractive index modulation for x = 0 and 0.10, and metal-insulator modulation for x = 0.28, 0.50, and 0.70, facilitated by the V_g-induced P → P changes for $x \le 0.28$ and the P → BM transformation for $x \ge 0.50$, as seen in Figure 4c–f. These observations agree with the V_g-induced changes in I_{SD} and ρ(300 K) in Figure 4a,b. Focusing on the detailed refractive index trends in gated LSCO, we first observe in Figure 5a that the k of LCO and LSCO films with x = 0.10 and 0.28 reaches a maximum near 420 nm, then steadily decrease at longer wavelengths. The absorption is nearly identical in all three cases, which is unsurprising given the clear similarities in structure, but the absorption peak slightly decreases in magnitude and blueshifts with increasing x, and x = 0.28 LSCO also shows a slight broadening in absorption. Through similar Kramers–Kronig-related arguments as employed above, these light absorption trends in $x \le 0.28$ gated LSCO films translate to the real index trends observed in Figure 5b, namely an n that is slightly blueshifted and lower in magnitude between

LCO and $x = 0.10$ LSCO, followed by an n of $x = 0.28$ that is slightly more dispersive and higher-index in the infrared due to the broadened absorption peak.

Shifting to BM LSCO at $x \geq 0.50$, we now observe the presence of two absorption peaks in $x = 0.50$ and 0.70 gated LSCO, and in as-grown BM SCO. Specifically, we see a stronger, shorter-wavelength peak that occurs at similar wavelengths to the single absorption peak in $x \leq 0.28$ LSCO, as well as a second, broader absorption peak centered at ≈750–900 nm. As x increases from 0.50 to 1.00, both absorption peaks slightly redshift and increase in magnitude, with much larger absorption changes in the shorter-wavelength peak. While n decreases slightly from $x = 0.50$ to 0.70 at visible wavelengths, the absorption trends in BM LSCO generally translate to increases in n between $x = 0.50$ to 1.00 compositions, as expected.

Finally, we note that the presence of one vs. two absorption features in $x \leq 0.28$ vs. $x \geq 0.50$ gated LSCO further aligns with the presence of disordered vs. ordered oxygen vacancies in these compositions, as described in conjunction with Figure 4. Firstly, the presence of two absorption peaks in the visible and near-infrared is a common optical signature for BM order, related to Co ions in both tetrahedral (*tet*) and octahedral (*oct*) coordination, as seen in our as-grown SCO film (Figure 5a, bottom panel) and in prior experimental optical studies of BM SCO films.[51,71,75] This further reinforces our observation from Figure 4 of full BM order in $x = 0.50$ and $x = 0.70$ LSCO, but a lack thereof in $x \leq 0.28$ LSCO. Previous studies of BM SCO assert that the shorter-wavelength feature is due to an interband transition from the O^{2p} orbital to a mostly-octahedral Co^{3d} orbital and that the longer-wavelength feature is due to an intraband transition between Co^{3d} orbitals.[51,71,75] Based on this picture, it is reasonable that the O^{2p}-$Co^{3d,oct}$ transition is present in gated LSCO at all x (as it was also observed in P LSCO based on our previous discussion), and does not involve the $Co^{3d,tet}$ orbital, which arises from BM ordering. Still, the slightly stronger and broader absorption of $x = 0.28$ relative to $x = 0$ and 0.10 suggests the formation of some $Co^{3d,tet}$ regions due to oxygen vacancies (Figure 4f), and therefore the possibility of Co^{3d} intraband transitions even at $x \leq 0.28$.

2.5. Electrochemically Gated LSCO for Infrared Active Metasurfaces

In the final section of this paper, we place the refractive index modulation observed in electrochemically gated LSCO in the broader context of active metasurfaces, specifically for the infrared. First, we return to the observation that electrochemically gated LSCO is capable of both insulator-insulator ($x = 0$, 0.10) and metal-insulator ($x = 0.28$, 0.50, 0.70) voltage-driven refractive index modulation, stemming from the combination of the x-dependent percolation insulator-metal transition in as-grown P LSCO and the significant electrochemical reduction induced by electrolyte gating. For additional emphasis on this point, the refractive index of as-grown P and gated LSCO at each x are plotted together in Figure S5, Supporting Information. To better quantify these voltage-induced refractive index changes at all x, Figure 5c,d shows the index modulation (Δn) and loss modulation (Δk) in LSCO, grouped by compositions that show insulator-insulator and metal-insulator contrast, respectively. In Figure 5c, we observe significant index modulation in low-x LSCO (≈0.6 for LCO and up to 1.3 for $x = 0.10$ LSCO in the infrared). The refractive indices themselves of LCO and $x = 0.10$ LSCO are attractive, with both compositions displaying high index ($n > 2.5$) with moderate to low loss ($k < 1.0$) throughout the infrared, both before and after gating. Based on these attributes, $x \leq 0.10$ LSCO can be compared with chalcogenide alloys such as GST, which transform between an $n > 3.5$ amorphous phase and an $n > 6$ crystalline phase, with both phases showing moderate to low loss in the infrared.[12,16,17] While electrochemically gated LCO and $x = 0.10$ LSCO show both lower index and lower index modulation than GST, these compositions can still tune the optical response of metamaterials significantly, as seen in the case of electrochemical modulation of lower-index TiO_2.[24] Analogously, in Figure 5d, we observe significant loss modulation (Δk) in LSCO at $x = 0.28$, 0.50, and 0.70, due to the opening of an electronic bandgap during gating, with the gated phases of these compositions again showing high index and low loss. These metal-insulator transitions are reminiscent of similar changes in VO_2 and $SmNiO_3$, where the insulating phase of each material supports resonant effects in many metamaterial geometries, but the strong optical loss in the metallic phase removes the resonance.[19,22,25] In LSCO, however, we observe for the first time the ability to achieve both types of refractive index modulation using a single material system, along with the significant additional convenience of non-volatile, low power, room-temperature phase changes.

To clearly illustrate the significant modulation achievable with electrochemically gated LSCO, we used finite-difference time-domain (FDTD) simulations to design a tunable plasmonic metasurface for these two different cases, using the refractive indices measured for LCO and $x = 0.50$ LSCO (**Figure 6**). As shown in Figure 6a, the chosen structure consists of a metal-insulator-metal geometry, comprised of a thin film of LSCO sandwiched between an Au nanodisk metasurface and an optically-thick Au back reflector. These FDTD simulations were performed without the ion gel to capture the ex situ modulation discussed throughout this study, but future demonstrations that include the ion gel are certainly feasible, as they can be designed to avoid absorption bands in the gel.[76] To understand how LSCO's refractive index changes affect the resonance of the plasmonic nanostructure, we plot the local electric field intensity normalized to that of the incident plane wave ($|E|^2/|E_0|^2$) around the cross-section of a single nanodisk before and after gating for LCO (Figure 6b) and $x = 0.50$ LSCO (Figure 6c). In Figure 6b, it is evident that both as-grown ($V_g = 0$ V) and gated ($V_g = 3.5$ V) LCO support a surface plasmon resonance in the Au nanodisk. Upon gating, the spectrum blueshifts ($\Delta\lambda = 600$ nm) and there is a slight increase in electric field intensity, which occur because of the decrease in both index and loss in LCO upon gating. This same metasurface absorber behaves very differently for the case of $x = 0.50$ LSCO, however, as shown in Figure 6c. Here, the field profiles for as-grown ($V_g = 0$ V) and gated ($V_g = 3.5$ V) LSCO show that at a single mid-infrared wavelength, the surface plasmon resonance can be turned "off" and "on" owing to the substantial contrast between the highly lossy metallic P phase and the high-index, low-loss BM phase.

In the rest of Figure 6, we show how this voltage-tunable metasurface resonance – when extended to the whole nanodisk array – creates significant mid-infrared reflectance modulation

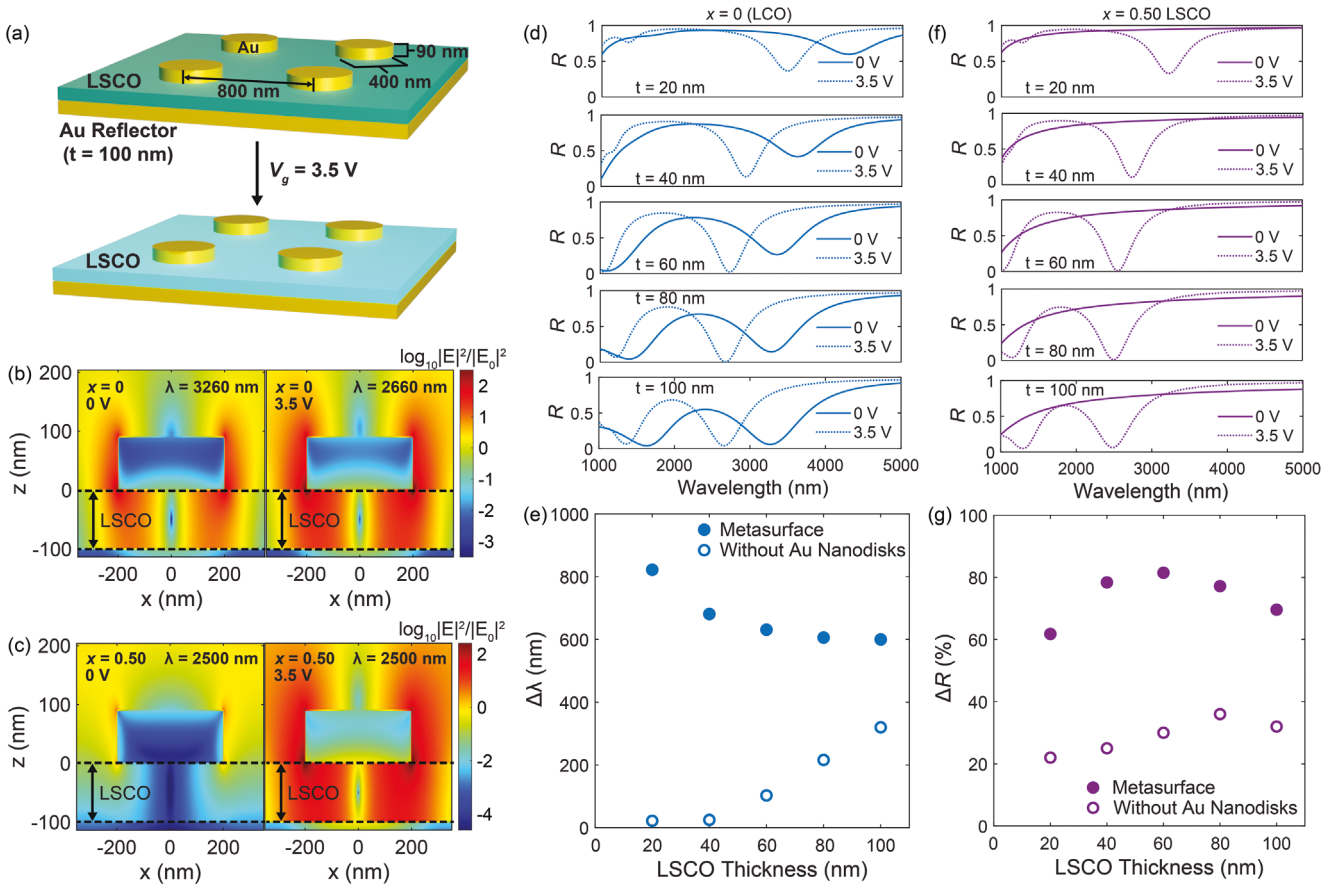

Figure 6. a) Schematic depiction of a tunable plasmonic absorber metasurface utilizing the electrolyte-gate-induced refractive index changes in LSCO, modeled with FDTD simulations. The LSCO layer was varied in terms of composition ($x = 0$ or 0.50) and thickness (20–100 nm). The thickness of the Au reflector was fixed at 100 nm in all cases. b,c) Cross-sections of the nanodisk metasurface used in FDTD simulations, showing local electric field intensity (E^2) normalized to the intensity of the incident plane wave ($E_0{}^2$) for b) $x = 0$ and c) $x = 0.50$ LSCO. In each case, the left panels show the fields with as-grown LSCO ($V_g = 0$ V) and the right panels show fields with gated LSCO ($V_g = 3.5$ V). d) Simulated wavelength-dependent reflectance spectra of the plasmonic absorber with as-grown ($V_g = 0$ V) and gated ($V_g = 3.5$ V) $x = 0$ LSCO (LCO), as the LSCO channel thickness increases from 20–100 nm. e) Resonant wavelength shift of the plasmonic metasurface between as-grown ($V_g = 0$ V) and gated ($V_g = 3.5$ V) $x = 0$ LSCO at different film thicknesses, shown in the filled circles. Open circles denote the shift in the resonant wavelength achieved at shorter wavelengths for the case with no nanodisks present. f) Simulated wavelength-dependent reflectance spectra of the plasmonic metasurface with as-grown ($V_g = 0$ V) and gated ($V_g = 3.5$ V) $x = 0.50$ LSCO, as the LSCO channel thickness increases from 20–100 nm. g) Single-wavelength reflectance modulation of the plasmonic metasurface between as-grown ($V_g = 0$ V) and gated ($V_g = 3.5$ V) $x = 0.50$ LSCO at different film thicknesses, shown as filled circles. Open circles denote the change in reflectance for the corresponding case without nanodisks.

in the far-field, even at LSCO film thicknesses as low as 20 nm. First considering the case of LCO, we observe in the top panel of Figure 6d that both as-grown ($V_g = 0$ V) and gated ($V_g = 3.5$ V) LCO films of 20 nm thickness produce distinct minima in an otherwise high reflectance (R) spectrum, again accompanied by a significant resonant wavelength blueshift of $\Delta\lambda = 822$ nm upon gating, for similar reasons as described above. As the thickness of the LCO layer increases from 20 to 100 nm (Figure 6d, lower panels), we observe the same blueshift and strengthening of the reflectance minimum from 0 to 3.5 V in each case, but also an overall strengthening of both reflectance minima as thickness increases. In fact, the resonance supported by 60-nm-thick gated LCO (Figure 6d, middle panel) becomes so strong that the reflectance becomes nearly zero ($R \approx 0.02$) near 2700 nm, thus signifying perfect light absorption in the metasurface; in 100-nm-thick LCO we observe near-perfect absorption at both 0 and 3.5 V. We also observe in Figure 6d an overall blueshift of the reflectance minima with increasing LCO thickness. We attribute this thickness-dependent effect to the cavity-like nature of this geometry, in which a larger LSCO thickness blueshifts the resonance.[8,77] Aside from these details, we emphasize that electrochemical gating of LCO films produces significant wavelength shifts ($\Delta\lambda$) in the reflectance spectra of plasmonic metasurfaces, regardless of film thickness, as shown by the filled circles in Figure 6e. This $\Delta\lambda$ is much larger than what is achievable solely based on thin-film interference between the LCO film and the Au back-reflector, which together form an asymmetric Fabry–Perót cavity[78] (open circles in Figure 6e). These thin film modes are responsible for the reflectance minima at shorter wavelengths (< 1200 nm) observed in Figure 6d, and are more clearly displayed in Figure S6, Supporting Information. However, the lower $\Delta\lambda$ observed in the thin film resonance is partly due to its location

at shorter wavelengths, where the refractive index modulation in LCO is not as high (Figure 5c). Nevertheless, the presence of the Au nanodisk metasurface is clearly instrumental in producing significant $\Delta\lambda$ and in pushing the resonant wavelengths into the mid-infrared.

Next, considering the case of reflectance modulation using $x = 0.50$ LSCO, Figure 6f shows that turning the plasmonic nanostructure resonance "off" and "on" translates to high broadband reflectance with metallic as-grown LSCO ($V_g = 0$ V), vs. a resonance-induced reflectance minimum with insulating gated LSCO ($V_g = 3.5$ V). Even an LSCO thickness as low as 20 nm supports reflectance modulation of $\Delta R > 60\%$ near 3200 nm (Figure 6f, top panel). As the LSCO thickness increases to 100 nm, we observe a trend similar to that in LCO, in which the insulating LSCO-supported resonance blueshifts and strengthens to the point of near-perfect light absorption. We also find a thickness-dependent decrease in reflectance for the $V_g = 0$ V (as-grown LSCO) case as light traverses a progressively larger optical path length, leading to more absorption by the metallic LSCO film. Figure 6g further emphasizes that electrochemically induced changes in $x = 0.50$ significantly modulate mid-infrared reflectance (ΔR) at a single wavelength, regardless of the specific film thickness in the range studied here. Analogous to LCO, Figure 6g also shows that this geometry enables over twice the ΔR observed from thin film reflectance modulation alone, again with the caveat that ΔR is lower for thin film resonances due to lower refractive index modulation at shorter wavelengths.

Finally, we comment more broadly on the potential for active metasurfaces based on the room-temperature, nonvolatile refractive index changes obtained in electrochemically gated LSCO. While LSCO can be realized in many other geometries, even the single plasmonic nanostructure shown here has numerous potential applications, particularly in the mid-infrared. A tunable plasmonic absorber featuring insulator-insulator modulation in LSCO could achieve dynamic thermal imaging/detection, for example, in which a single "pixel" is voltage-tuned to several wavelengths, corresponding to different temperatures.[15,16,18] Metal-insulator modulation in LSCO could also be used for adaptive camouflage,[79] in which one could switch between being "seen" (metallic LSCO) to "invisible" (insulating LSCO). Other applications, possibly in the near-infrared, include chemical sensing based on analyte-induced resonant wavelength shifts[80] (insulator-insulator modulation) and optical memory devices in which different light intensities can be encoded at a single wavelength (metal-insulator modulation).[59] We are confident that these applications can be experimentally realized in our proposed structure, where an epitaxial metallic film that is lattice-matched to LSCO could serve as a back reflector instead of Au. To enable these applications, electrochemically induced transitions in LSCO will require significant reversibility, switching frequency, and endurance; there is substantial evidence, however, that these advances are possible. Reversibility over several cycles has been demonstrated for the P ↔ BM transformation in SCO[43,51,52] and will be the focus of a future study of ours on $x = 0.50$ LSCO. Simple theoretical estimates of switching frequencies (i.e., by calculating diffusion times using reported values of oxygen vacancy diffusivity[34] and assuming ≈10 nm film thickness) suggest potential operation at 1 Hz or more, particularly with top-gate geometries. Thus, we believe the work presented here sets the stage for the proliferation of infrared-active metasurfaces based on both insulator-insulator and metal-insulator reversible refractive index modulation in electrochemically gated LSCO.

3. Conclusion

We have presented comprehensive optical studies of ion-gel-gated epitaxial $La_{1-x}Sr_xCoO_{3-\delta}$ (LSCO) films across nearly the entire phase diagram ($0 \le x \le 0.70$), highlighting key insights from structural/electronic transport measurements, and motivating the use of electrochemically gated LSCO for tunable nanophotonic applications such as active metasurfaces. Kramers-Kronig-consistent complex refractive index models of as-grown, perovskite-phase LSCO films show optical absorption trends consistent with the percolation insulator-metal transition that occurs in perovskite LSCO at $x = 0.18$. LSCO films at all x experience significant refractive index changes upon positive-voltage electrochemical gating, where films with $x \le 0.10$ show insulator-insulator modulation between two high-index insulating perovskite phases, and films with $x \ge 0.28$ show metal-insulator modulation accompanied by a topotactic perovskite to brownmillerite phase transformation for $x = 0.50$ and 0.70. To illustrate the power of LSCO's refractive index changes to induce significant optical modulation in active metasurfaces, we then used the refractive index models for LCO and $x = 0.50$ LSCO to perform FDTD simulations of a tunable plasmonic metasurface. These simulations highlight the potential ability to shift a mid-infrared spectrum by $\Delta\lambda > 600$ nm using insulator-insulator modulation in LCO and to modulate mid-infrared reflectance by $\Delta R > 60\%$ using metal-insulator modulation in $x = 0.50$ LSCO. Given the significant, nonvolatile, room-temperature effects, and the diverse sets of refractive index changes at various x, electrochemically gated LSCO can be utilized as a library of tunable photonic materials for infrared active metasurfaces, potentially enabling diverse applications such as dynamic thermal imaging, camouflage, and optical memory devices.

4. Experimental Section

LSCO films with $0 \le x \le 0.70$, along with BM SCO films ($x = 1.00$), were deposited on $(LaAlO_3)_{0.3}(Sr_2TaAlO_6)_{0.7}$ (001) (LSAT) substrates using high-pressure-oxygen sputtering using previously-optimized conditions.[46–48,61,62,64] First, 10 × 10 × 0.5 mm commercial LSAT(001) substrates from MTI were annealed at 900 °C under 1 Torr of ultra-high-purity (99.998%) O_2 for 15 min. LSCO films with $0 \le x \le 0.70$ were then sputtered from polycrystalline ceramic LSCO targets at 600 °C substrate temperature (700 °C in the case of $x = 0$[62]), 45–65 W of DC power, and 1.5 Torr O_2 pressure, after which the films were cooled to room temperature in 600 Torr O_2 pressure. BM SCO films were grown at a substrate temperature of 700 °C using 40 W of DC power and cooled to room temperature at the growth pressure of 1.5 Torr O_2. The resulting LSCO films ranged from 12–22 nm in thickness across all compositions, as determined from wide-angle XRD Laue fringes. All LSCO films at a particular composition were grown under identical conditions and therefore have the same thickness within ≈0.5 nm. LSCO films were grown on both one- and two-side polished LSAT substrates to enable subsequent spectroscopic ellipsometry measurements and intensity reflection/transmission measurements, respectively.

Electric double-layer transistors (EDLTs) based on LSCO were fabricated following established methods.[46–48] 3.5 × 4.0 mm^2 center channels in the LSCO film were first defined with Ar ion milling using a steel mask.

Mg (5 nm)/Pt (50 nm) films were then deposited through a second mask to form the source, drain, and gate electrodes, and subsequently rapid-thermal-annealed at 450 °C for 10 min in flowing O_2. As shown in Figure 1b of the main text, the EDLTs were fabricated in a side-gate geometry so that the LSCO channel could be probed by XRD and various optical spectroscopy techniques. The ion gel electrolytes used for gating experiments consisted of the ionic liquid 1-ethyl-3-methylimidazolium bis(trifluoromethylsulfonyl)amide (EMI:TFSI) embedded in poly(vinylidene fluoride-co-hexafluoropropylene) (P(VDF-HFP)).[81] Using acetone as the solvent, a 1:4:7 by-weight mixture of polymer:ionic liquid:solvent was spin-coated onto glass wafers, then treated under vacuum at 70 °C to remove the solvent.[81] The "cut-and-stick" nature of these ion gels allows one to easily cut sections of the dried gels with a blade and use tweezers to apply them directly onto the device, completing the EDLTs.[81]

Electrolyte gating experiments and temperature-dependent resistivity measurements of LSCO EDLTs were performed in a Quantum Design Physical Property Measurement System and a closed-cycle He refrigerator. Keithley 2400 source-measure units were used to measure channel resistances and apply gate voltages. All gating experiments were performed under the identical conditions of 300 K and vacuum ($< 10^{-5}$ Torr). The gating was accomplished by sweeping V_g from 0 V to +3.5 V at a sweep rate of 0.5 mV s^{-1}, during which in situ source-drain current measurements were also obtained with a constant source-drain voltage (V_{SD}) of 0.2 V, and in situ gate current measurements were concurrently made between the gate electrodes (working electrode) and source-drain electrodes (counter electrode). Ex situ high-resolution wide-angle X-ray diffraction was performed using a Rigaku Smartlab XE diffractometer with a 5-axis goniometer, HyPix-3000 high energy resolution detector, ≈1.54 Å (Cu Kα) incident wavelength, and a spot size of 2×2 mm^2. STEM samples were prepared using an FEI Helios Nanolab G4 dual-beam focused ion beam (FIB) microscope. The sample was coated with amorphous carbon prior to ion beam exposure in the FIB, to prevent damage to the film surface. The sample was first thinned using 30 keV Ga ion beams followed by a 2 keV ion beam shower to remove damaged surface layers. HAADF-STEM imaging was performed on an aberration-corrected FEI Titan G2 60–300 (S)TEM which is equipped with a monochromator and a CEOS-DCOR probe corrector. The microscope was operated at 200 keV, with a probe current of 100 pA and probe convergence angle of 18.2 mrad. The HAADF detector inner and outer collection angles used were 58.5 and 200 mrad, respectively.

All optical measurements were performed ex-situ under ambient conditions. Spectroscopic ellipsometry was performed on LSCO EDLTs grown on one-side polished substrates using a J.A. Woollam VASE ellipsometer in the wavelength range of 350–1100 nm. Unless otherwise specified, all ellipsometric measurements were performed at a 40° incident angle, which produces a spot width small enough (< 4 mm) to probe only the LSCO channel and not the surrounding electrodes. Separately, optical transmittance measurements were performed on LSCO EDLTs grown on two-side polished substrates. Transmittance data from 350–2500 nm were collected using a Cary 7000 UV–vis–NIR spectrophotometer, where samples were mounted on an opaque holder with an opening smaller than 3.5×4.0 mm^2 in area such that only the LSCO channel was illuminated. Transmittance data from 2500–5000 nm were collected using a Bruker Hyperion 2000 FTIR microscope with a liquid N_2-cooled MCT detector coupled to a Bruker Invenio-R FTIR spectrometer. All transmittance spectra were collected at normal incidence using unpolarized light and were normalized to the transmittance of air. For each composition of LSCO, the corresponding transmittance data were loaded into the J. A. Woollam ellipsometry software, and both the ellipsometric and transmittance data for that composition were then fit together to Kramers-Kronig-consistent refractive index models of LSCO ranging from 350–5000 nm following a previously-demonstrated technique.[82] To enable this fitting process for LSCO, the refractive index of each two-side-polished LSAT substrate used for this study was separately modeled in a similar manner.

FDTD simulations of LSCO plasmonic metasurfaces (depicted in Figure 6a) were performed using Ansys Lumerical software. These metal-insulator-metal structures consisted of an array of Au nanodisks, a planar LSCO layer, and a planar Au reflector on the bottom. For all FDTD simulations, the Au nanodisks were modeled with 400 nm diameter, 90 nm height, and 800 nm pitch, the LSCO thickness was varied from 20–100 nm, and the Au reflector thickness was fixed at 100 nm. The ion gel was not included in the model in order to model ex situ modulation, mirroring the optical studies presented here. A broadband plane wave source was injected in the *z*-direction, periodic boundary conditions were used in the *x*- and *y*-directions, and perfectly matched layers were used as boundary conditions in the *z*-direction. The refractive index of LSCO was directly taken from the oscillator models developed in this study, and the refractive index of Au was taken from the literature.[83] To model the same structure without the Au nanodisks present (Figure S6, Supporting Information and Figure 6e,g), the reflectance spectra of LSCO films of different *x* and thickness on optically-thick (100 nm) Au were calculated with open-source MATLAB code designed for transfer-matrix modeling, using the same refractive indices described above.[84]

Supporting Information

Supporting Information is available from the Wiley Online Library or from the author.

Acknowledgements

This work was supported primarily by the National Science Foundation through the University of Minnesota MRSEC under Award Number DMR-2011401. Parts of this work were performed in the Characterization Facility at the University of Minnesota, which receives partial support from NSF through the MRSEC program. Portions of this work were also conducted in the Minnesota Nano Center, which is supported by NSF through the National Nano Coordinated Infrastructure (NNCI) under Award Number ECCS-2025124. The authors acknowledge Turan Birol and Amartyajyoti Saha at the University of Minnesota for helpful discussions regarding the electronic band structure of LSCO. C.L. and V.E.F. conceived of the study and oversaw its execution. R.D.C. deposited the films, did the structural characterization and optical characterization, and performed the simulations under the guidance of V.E.F. R.D.C. performed the electrolyte gating measurements and analyses in collaboration with W.M.P. and under the guidance of C.L. R.D.C. and W.M.P. performed the temperature-dependent resistivity measurements together under the guidance of C.L. S.G. performed the STEM measurements in collaboration with R.D.C. under the guidance of K.A.M. R.D.C. and V.E.F. wrote the paper with input from all authors.

Conflict of Interest

The authors declare no conflict of interest.

Data Availability Statement

The data that support the findings of this study are openly available in DRYAD at https://doi.org/10.5061/dryad.p8cz8w9v9.

Keywords

active metasurfaces, electrolyte gating, insulator-insulator transitions, metal-insulator transitions, mid-infrared, perovskite oxide, phase-change photonic materials

Received: January 13, 2023
Revised: April 13, 2023
Published online:

[1] D. R. Smith, *Science* **2004**, *305*, 788.
[2] S. P. Burgos, R. de Waele, A. Polman, H. A. Atwater, *Nat. Mater.* **2010**, *9*, 407.
[3] Z. Li, P. Lin, Y.-W. Huang, J.-S. Park, W. T. Chen, Z. Shi, C.-W. Qiu, J.-X. Cheng, F. Capasso, *Sci. Adv.* **2021**, *7*, abe4458.
[4] P. Berini, *ACS Photonics* **2022**, *9*, 2204.
[5] P. Thureja, R. Sokhoyan, C. U. Hail, J. Sisler, M. Foley, M. Y. Grajower, H. A. Atwater, *Nanophotonics* **2022**, *11*, 3745.
[6] Y.-W. Huang, H. W. H. Lee, R. Sokhoyan, R. A. Pala, K. Thyagarajan, S. Han, D. P. Tsai, H. A. Atwater, *Nano Lett.* **2016**, *16*, 5319.
[7] H. Zhao, R. Zhang, H. T. Chorsi, W. A. Britton, Y. Chen, P. P. Iyer, J. A. Schuller, L. D. Negro, J. Klamkin, *Nanophotonics* **2019**, *8*, 1803.
[8] Y. Lee, J. Yun, S. Kim, M. Seo, S. In, H. Jeong, S. Lee, N. Park, T. D. Chung, B. Lee, *Adv. Opt. Mater.* **2020**, *8*, 2001256.
[9] G. K. Shirmanesh, R. Sokhoyan, P. C. Wu, H. A. Atwater, *ACS Nano* **2020**, *14*, 6912.
[10] J. Kim, H. Son, D. J. Cho, B. Geng, W. Regan, S. Shi, K. Kim, A. Zettl, Y.-R. Shen, F. Wang, *Nano Lett.* **2012**, *12*, 5598.
[11] N. Dabidian, I. Kholmanov, A. B. Khanikaev, K. Tatar, S. Trendafilov, S. H. Mousavi, C. Magnuson, R. S. Ruoff, G. Shvets, *ACS Photonics* **2015**, *2*, 216.
[12] A. Nemati, G. Yuan, J. Deng, A. Huang, W. Wang, Y. T. Toh, J. Teng, Q. Wang, *Adv. Opt. Mater.* **2022**, *10*, 2101847.
[13] S. Abdollahramezani, O. Hemmatyar, M. Taghinejad, H. Taghinejad, A. Krasnok, A. A. Eftekhar, C. Teichrib, S. Deshmukh, M. A. El-Sayed, E. Pop, M. Wuttig, A. Alù, W. Cai, A. Adibi, *Nat. Commun.* **2022**, *13*, 1696.
[14] Y. Zhang, C. Fowler, J. Liang, B. Azhar, M. Y. Shalaginov, S. Deckoff-Jones, S. An, J. B. Chou, C. M. Roberts, V. Liberman, M. Kang, C. Ríos, K. A. Richardson, C. Rivero-Baleine, T. Gu, H. Zhang, J. Hu, *Nat. Nanotechnol.* **2021**, *16*, 661.
[15] A. Tittl, A.-K. U. Michel, M. Schäferling, X. Yin, B. Gholipour, L. Cui, M. Wuttig, T. Taubner, F. Neubrech, H. Giessen, *Adv. Mater.* **2015**, *27*, 4597.
[16] A. Leitis, A. Heßler, S. Wahl, M. Wuttig, T. Taubner, A. Tittl, H. Altug, *Adv. Funct. Mater.* **2020**, *30*, 1910259.
[17] M. Wuttig, H. Bhaskaran, T. Taubner, *Nat. Photonics* **2017**, *11*, 465.
[18] B. Gholipour, J. Zhang, K. F. MacDonald, D. W. Hewak, N. I. Zheludev, *Adv. Mater.* **2013**, *25*, 3050.
[19] L. Liu, L. Kang, T. S. Mayer, D. H. Werner, *Nat. Commun.* **2016**, *7*, 13236.
[20] A. M. Boyce, J. W. Stewart, J. Avila, Q. Shen, S. Zhang, V. D. Wheeler, M. H. Mikkelsen, *Nano Lett.* **2022**, *22*, 3525.
[21] Y. Kim, P. C. Wu, R. Sokhoyan, K. Mauser, R. Glaudell, G. Kafaie Shirmanesh, H. A. Atwater, *Nano Lett.* **2019**, *19*, 3961.
[22] Z. Zhu, P. G. Evans, R. F. Haglund, J. G. Valentine, *Nano Lett.* **2017**, *17*, 4881.
[23] A. Howes, Z. Zhu, D. Curie, J. R. Avila, V. D. Wheeler, R. F. Haglund, J. G. Valentine, *Nano Lett.* **2020**, *20*, 4638.
[24] J. Eaves-Rathert, E. Kovalik, C. F. Ugwu, B. R. Rogers, C. L. Pint, J. G. Valentine, *Nano Lett.* **2022**, *22*, 1626.
[25] Z. Li, Y. Zhou, H. Qi, Q. Pan, Z. Zhang, N. N. Shi, M. Lu, A. Stein, C. Y. Li, S. Ramanathan, N. Yu, *Adv. Mater.* **2016**, *28*, 9117.
[26] M. Huang, A. Jun Tan, F. Büttner, H. Liu, Q. Ruan, W. Hu, C. Mazzoli, S. Wilkins, C. Duan, J. K. W. Yang, G. S. D. Beach, *Nat. Commun.* **2019**, *10*, 5030.
[27] Y. Li, J. van de Groep, A. A. Talin, M. L. Brongersma, *Nano Lett.* **2019**, *19*, 7988.
[28] L. McRae, Y. Xie, B. Gholipour, *Adv. Opt. Mater.* **2021**, *9*, 2101046.
[29] E. Klopfer, S. Dagli, D. Barton, M. Lawrence, J. A. Dionne, *Nano Lett.* **2022**, *22*, 1703.
[30] Y. Lee, M.-K. Park, S. Kim, J. H. Shin, C. Moon, J. Y. Hwang, J.-C. Choi, H. Park, H.-R. Kim, J. E. Jang, *ACS Photonics* **2017**, *4*, 1954.
[31] D. Franklin, Y. Chen, A. Vazquez-Guardado, S. Modak, J. Boroumand, D. Xu, S.-T. Wu, D. Chanda, *Nat. Commun.* **2015**, *6*, 7337.
[32] C. Wan, Z. Zhang, D. Woolf, C. M. Hessel, J. Rensberg, J. M. Hensley, Y. Xiao, A. Shahsafi, J. Salman, S. Richter, Y. Sun, M. M. Qazilbash, R. Schmidt-Grund, C. Ronning, S. Ramanathan, M. A. Kats, *Ann. Phys.* **2019**, *531*, 1900188.
[33] M. Currie, M. A. Mastro, V. D. Wheeler, *Opt. Mater. Express* **2017**, *7*, 1697.
[34] C. Leighton, T. Birol, J. Walter, *APL Mater.* **2022**, *10*, 040901.
[35] C. Leighton, *Nat. Mater.* **2019**, *18*, 13.
[36] S. Z. Bisri, S. Shimizu, M. Nakano, Y. Iwasa, *Adv. Mater.* **2017**, *29*, 1607054.
[37] K. Xu, S. K. Fullerton-Shirey, *J. Phys. Mater.* **2020**, *3*, 032001.
[38] J. T. Ye, Y. J. Zhang, R. Akashi, M. S. Bahramy, R. Arita, Y. Iwasa, *Science* **2012**, *338*, 1193.
[39] S. H. Kim, K. Hong, W. Xie, K. H. Lee, S. Zhang, T. P. Lodge, C. D. Frisbie, *Adv. Mater.* **2013**, *25*, 1822.
[40] X. Ren, Y. Wang, Z. Xie, F. Xue, C. Leighton, C. D. Frisbie, *Nano Lett.* **2019**, *19*, 4738.
[41] S. Ning, Q. Zhang, C. Occhialini, R. Comin, X. Zhong, C. A. Ross, *ACS Nano* **2020**, *14*, 8949.
[42] H. Wang, J. Walter, K. Ganguly, B. Yu, G. Yu, Z. Zhang, H. Zhou, H. Fu, M. Greven, C. Leighton, *Phys. Rev. Mater.* **2019**, *3*, 075001.
[43] B. Cui, C. Song, F. Li, X. Y. Zhong, Z. C. Wang, P. Werner, Y. D. Gu, H. Q. Wu, M. S. Saleem, S. S. P. Parkin, F. Pan, *Phys. Rev. Appl.* **2017**, *8*, 044007.
[44] B. M. Lefler, W. M. Postiglione, C. Leighton, S. J. May, *Adv. Funct. Mater.* **2022**, *32*, 2208434.
[45] H. Wang, W. M. Postiglione, V. Chaturvedi, E. L. Runnerstrom, A. Cleri, J. Nordlander, J.-P. Maria, C. Leighton, *APL Mater.* **2022**, *10*, 121106.
[46] J. Walter, H. Wang, B. Luo, C. D. Frisbie, C. Leighton, *ACS Nano* **2016**, *10*, 7799.
[47] J. Walter, G. Yu, B. Yu, A. Grutter, B. Kirby, J. Borchers, Z. Zhang, H. Zhou, T. Birol, M. Greven, C. Leighton, *Phys. Rev. Mater.* **2017**, *1*, 071403.
[48] V. Chaturvedi, W. M. Postiglione, R. D. Chakraborty, B. Yu, W. Tabiś, S. Hameed, N. Biniskos, A. Jacobson, Z. Zhang, H. Zhou, M. Greven, V. E. Ferry, C. Leighton, *ACS Appl. Mater. Interfaces* **2021**, *13*, 51205.
[49] G. H. Jonker, J. H. Van Santen, *Physica* **1953**, *19*, 120.
[50] J. Wu, C. Leighton, *Phys. Rev. B* **2003**, *67*, 174408.
[51] N. Lu, P. Zhang, Q. Zhang, R. Qiao, Q. He, H.-B. Li, Y. Wang, J. Guo, D. Zhang, Z. Duan, Z. Li, M. Wang, S. Yang, M. Yan, E. Arenholz, S. Zhou, W. Yang, L. Gu, C.-W. Nan, J. Wu, Y. Tokura, P. Yu, *Nature* **2017**, *546*, 124.
[52] Q. Lu, S. Huberman, H. Zhang, Q. Song, J. Wang, G. Vardar, A. Hunt, I. Waluyo, G. Chen, B. Yildiz, *Nat. Mater.* **2020**, *19*, 655.
[53] H. M. Aarbogh, J. Wu, L. Wang, H. Zheng, J. F. Mitchell, C. Leighton, *Phys. Rev. B* **2006**, *74*, 134408.
[54] S. Yamaguchi, Y. Okimoto, K. Ishibashi, Y. Tokura, *Phys. Rev. B* **1998**, *58*, 6862.
[55] Y. Tokura, Y. Okimoto, S. Yamaguchi, H. Taniguchi, T. Kimura, H. Takagi, *Phys. Rev. B* **1998**, *58*, R1699.
[56] Q. Chen, X. Wang, M. Zhang, Z. Xu, J. Gong, A. Rahman, L. Fan, R. Dai, Z. Wang, Z. Zhang, *AIP Adv.* **2020**, *10*, 035117.
[57] D. W. Jeong, W. S. Choi, S. Okamoto, J.-Y. Kim, K. W. Kim, S. J. Moon, D.-Y. Cho, H. N. Lee, T. W. Noh, *Sci. Rep.* **2014**, *4*, 6124.
[58] W. W. Li, Z. G. Hu, Y. W. Li, M. Zhu, Z. Q. Zhu, J. H. Chu, *ACS Appl. Mater. Interfaces* **2010**, *2*, 896.
[59] M. D. Goldflam, M. K. Liu, B. C. Chapler, H. T. Stinson, A. J. Sternbach, A. S. McLeod, J. D. Zhang, K. Geng, M. Royal, B.-J. Kim, R. D. Averitt, N. M. Jokerst, D. R. Smith, H.-T. Kim, D. N. Basov, *Appl. Phys. Lett.* **2014**, *105*, 041117.

[60] M. A. Torija, M. Sharma, J. Gazquez, M. Varela, C. He, J. Schmitt, J. A. Borchers, M. Laver, S. El-Khatib, C. Leighton, *Adv. Mater.* **2011**, *23*, 2711.
[61] J. Walter, S. Bose, M. Cabero, M. Varela, C. Leighton, *Phys. Rev. Mater.* **2020**, *4*, 091401.
[62] V. Chaturvedi, J. Walter, A. Paul, A. Grutter, B. Kirby, J. S. Jeong, H. Zhou, Z. Zhang, B. Yu, M. Greven, K. A. Mkhoyan, T. Birol, C. Leighton, *Phys. Rev. Mater.* **2020**, *4*, 034403.
[63] J. Gazquez, S. Bose, M. Sharma, M. A. Torija, S. J. Pennycook, C. Leighton, M. Varela, *APL Mater.* **2013**, *1*, 012105.
[64] J. Walter, S. Bose, M. Cabero, G. Yu, M. Greven, M. Varela, C. Leighton, *Phys. Rev. Mater.* **2018**, *2*, 111404.
[65] M. A. Korotin, S. Y. Ezhov, I. V. Solovyev, V. I. Anisimov, D. I. Khomskii, G. A. Sawatzky, *Phys. Rev. B* **1996**, *54*, 5309.
[66] J.-H. Kwon, W. S. Choi, Y.-K. Kwon, R. Jung, J.-M. Zuo, H. N. Lee, M. Kim, *Chem. Mater.* **2014**, *26*, 2496.
[67] T. Arima, Y. Tokura, J. B. Torrance, *Phys. Rev. B* **1993**, *48*, 17006.
[68] S. Yamaguchi, Y. Okimoto, H. Taniguchi, Y. Tokura, *Phys. Rev. B* **1996**, *53*, R2926.
[69] W. S. Choi, H. Jeen, J. H. Lee, S. S. A. Seo, V. R. Cooper, K. M. Rabe, H. N. Lee, *Phys. Rev. Lett.* **2013**, *111*, 097401.
[70] M. A. Señarís-Rodríguez, J. B. Goodenough, *J. Solid State Chem.* **1995**, *118*, 323.
[71] J. H. Lee, W. S. Choi, H. Jeen, H.-J. Lee, J. H. Seo, J. Nam, M. S. Yeom, H. N. Lee, *Sci. Rep.* **2017**, *7*, 16066.
[72] H. Takahashi, F. Munakata, M. Yamanaka, *Phys. Rev. B* **1996**, *53*, 3731.
[73] D. I. Khomskii, G. A. Sawatzky, *Solid State Commun.* **1997**, *102*, 87.
[74] W. M. Postiglione, G. Yu, V. Chaturvedi, K. Heltemes, A. Jacobson, H. Zhou, M. Greven, C. Leighton, *in preparation*.
[75] J. Zhao, H. Guo, X. He, Q. Zhang, L. Gu, X. Li, K. Jin, T. Yang, C. Ge, Y. Luo, M. He, Y. Long, J. Wang, H. Qian, C. Wang, H. Lu, G. Yang, K. Ibrahim, *ACS Appl. Mater. Interfaces* **2018**, *10*, 10211.
[76] C. Li, Z. Su, J. Tan, Y. Xue, Y. Yang, H. Yin, G. Zhang, Q. Zhang, *J. Mater. Sci.* **2020**, *55*, 9119.
[77] J. B. Lassiter, F. McGuire, J. J. Mock, C. Ciracì, R. T. Hill, B. J. Wiley, A. Chilkoti, D. R. Smith, *Nano Lett.* **2013**, *13*, 5866.
[78] M. A. Kats, D. Sharma, J. Lin, P. Genevet, R. Blanchard, Z. Yang, M. M. Qazilbash, D. N. Basov, S. Ramanathan, F. Capasso, *Appl. Phys. Lett.* **2012**, *101*, 221101.
[79] O. Salihoglu, H. B. Uzlu, O. Yakar, S. Aas, O. Balci, N. Kakenov, S. Balci, S. Olcum, S. Süzer, C. Kocabas, *Nano Lett.* **2018**, *18*, 4541.
[80] S. K. Patel, J. Parmar, V. Sorathiya, T. K. Nguyen, V. Dhasarathan, *Sci. Rep.* **2021**, *11*, 7101.
[81] K. H. Lee, M. S. Kang, S. Zhang, Y. Gu, T. P. Lodge, C. D. Frisbie, *Adv. Mater.* **2012**, *24*, 4457.
[82] S. Niu, G. Joe, H. Zhao, Y. Zhou, T. Orvis, H. Huyan, J. Salman, K. Mahalingam, B. Urwin, J. Wu, Y. Liu, T. E. Tiwald, S. B. Cronin, B. M. Howe, M. Mecklenburg, R. Haiges, D. J. Singh, H. Wang, M. A. Kats, J. Ravichandran, *Nat. Photonics* **2018**, *12*, 392.
[83] A. D. Rakić, A. B. Djurišić, J. M. Elazar, M. L. Majewski, *Appl. Opt.* **1998**, *37*, 5271.
[84] U. Griesmann, A thin film multilayer toolbox for Octave and MATLAB https://github.com/ulfgri/tftb-toolbox (accessed: October 2021).